



High thermostable ordered mesoporous SiO₂–TiO₂ coated circulating-bed biofilm reactor for unpredictable photocatalytic and biocatalytic performance

Linlin Zhang^{a,b,1}, Zipeng Xing^{a,b,*}, Hang Zhang^b, Zhenzi Li^c, Xiaoyan Wu^c, Xiaodong Zhang^b, Yan Zhang^b, Wei Zhou^{a,**}

^a Key Laboratory of Functional Inorganic Material Chemistry, Ministry of Education of the People's Republic of China, Heilongjiang University, Harbin 150080, PR China

^b Key Laboratory of Chemical Engineering Process and Technology for High-Efficiency Conversion, College of Heilongjiang Province, Heilongjiang University, Harbin 150080, PR China

^c Department of Epidemiology and Biostatistics, Harbin Medical University, Harbin 150086, PR China

ARTICLE INFO

Article history:

Received 4 May 2015

Received in revised form 30 June 2015

Accepted 5 July 2015

Available online 13 July 2015

Keywords:

Ordered mesoporous SiO₂–TiO₂
Photocatalytic circulating-bed biofilm reactor
Photocatalysis coupled biocatalysis
High thermostability
Trichlorophenol

ABSTRACT

Utilizing high thermostable ordered mesoporous SiO₂–TiO₂ as a precursor, macroporous polyurethane foam (PUF) as a floating biofilm carrier, the photocatalytic circulating-bed biofilm reactor (PCBBR) is fabricated via ultrasonic vibration and deposition approach. The prepared SiO₂–TiO₂/PUF carrier is characterized in detail by X-ray diffraction, Raman spectroscopy, Fourier transform infrared spectroscopy, X-ray photoelectron spectroscopy, transmission electron microscopy, N₂ adsorption, scanning electron microscopy and energy dispersive spectroscopy. The results indicate that the ordered mesoporous SiO₂–TiO₂ network can be maintained and the presence of SiO₂ can inhibit the anatase-to-rutile phase transformation during 800 °C calcinations. Furthermore, the prepared SiO₂–TiO₂/PUF carrier presents a hierarchical macro/mesoporous structure, filling the bacterium to the channels. The PCBBR exhibits good synergic effect for the refractory phenolic wastewater, and the total organic carbon removal ratio of high toxic 2,4,5-trichlorophenol is up to 97.5% after hydraulic retention time for 3 h, which is ascribed to the hierarchical macro/mesoporous structure in favor of pollutants adsorption, efficient photon utilization and microorganism loading. This novel ordered mesoporous SiO₂–TiO₂ coated circulating-bed biofilm reactor is promising in the environmental field.

© 2015 Elsevier B.V. All rights reserved.

1. Introduction

With the rapid development of chemical industry and the resultant widespread use of chemicals, types of wastewater have been produced, which are potentially harmful to the environment [1–3]. There into, the phenolic wastewater that includes phenol and 2,4,5-Trichlorophenol (TCP) has been one of the major problems for decades. Phenolic compounds are examples of recalcitrant toxic pollutants presented in liquid waste streams from a variety of industries, such as those involved in production of steel, resins,

ceramics, fiberglass, fungicides and herbicides, metals, and textiles [4–6]. Especially, 2,4,5-TCP tends to bioaccumulate in the environment due to its biorecalcitrance in nature and in wastewater treatment plants [7].

Although phenol is relatively easy to be biodegraded, traditional biodegradation of phenol often is still inefficient, due to the self-inhibition for the high concentrations, the accumulation of intermediates of phenol metabolism, and the release of soluble microbial products. Even when the phenol is biodegraded, its kinetics is often slow, and biodegradation occurs only at low concentration due to the inhibition [8,9]. In contrast, advanced oxidation process (AOP) is a robust method to break down large organic molecules, including aromatic compounds. Among AOPs, photocatalytic oxidation is promising as a means to partly transform the complex structure of molecules like 2,4,5-TCP into biodegradable products [10]. Titanium dioxide (TiO₂) particles have excellent photocatalytic properties and applications which have

* Corresponding author at: Key Laboratory of Functional Inorganic Material Chemistry, Ministry of Education of the People's Republic of China, Heilongjiang University, Harbin 150080, PR China. Fax: +86 451 8660 8240.

** Corresponding author. Fax: +86 451 8660 8240.

E-mail addresses: xzplab@163.com (Z. Xing), zwchem@hotmail.com (W. Zhou).

¹ Fax: +86 451 8660 8240.

recently received great attentions owing to their chemical stability and high reactivity under UV light irradiation ($< 390\text{ nm}$) [11–13]. The produced hydroxyl radicals via charged holes (h^+) and excited electrons (e^-) are the main reactive species for oxidative/reductive degradation of a wide range of organic pollutants, and details of the degradation process have been extensively discussed [14–17]. However, full mineralization by the photocatalytic oxidation is economically prohibitive, and the products from partial photocatalytic oxidation retain toxicity and degradation demand [18].

An emerging approach combines photocatalysis and biocatalysis can overcome the limitations of both methods. For the combined treatment, the photocatalysis partially transforms biorecalcitrant organic compounds into intermediates that can be fully mineralized by biodegradation further. However, the problems of sequential treatment can be optimized and downsized if the photocatalysis and biodegradation occur together; this is called intimate coupling [19]. Marsolek et al. successfully demonstrates the concept of intimate coupling of photocatalysis and biodegradation (ICPB) for 2,4,5-TCP in a novel photocatalytic circulating-bed biofilm reactor (PCBBR) that exploits macro-porous cellulose carriers [20]. The biofilm in the PCBBR accumulates inside the macro porous carriers. TiO_2 particles are either fixed onto the outer surface of biofilm carriers or circulated in slurry form. While illuminated with UV light, the advanced oxidation process take place, which includes the photolysis or the TiO_2 photocatalysis. The bacteria are well protected from UV light, toxic substrates, free radicals, and physical loss, but are close to the advance-oxidation reactions so they can immediately degrade photo-catalytic products that are biodegradable. However, a key challenge of the PCBBR is the carrier that needs macroporous and light-weight. The carriers used by Marsolek et al. are made of cellulose, but they are charred by UV irradiation and hydroxyl radical attack. It eventually leads to a deterioration of the physical structure of carriers. Therefore, the biofilm-carrier needs to be made of a material better suited to intimate coupling with the photocatalysis. An ideal carrier for PCBBR should have porosity suitable for accumulating biofilm inside, a density allowing good circulation in the reactor, the ability to hold a substantial amount of TiO_2 , and durability for long-term use in the PCBBR [21,22]. Up to date, it is still a great challenge.

In this paper, we firstly prepared a high thermostable ordered mesoporous $\text{SiO}_2\text{--TiO}_2$ as the precursor, and coated on the macroporous PUF as a floating hierarchical macro/mesoporous biofilm carrier. It is well-known that high crystallinity of anatase TiO_2 , which possesses less surface defects, is one of the critical factors in improving photocatalysis [23,24]. However, the high crystallinity requires high calcinations temperature. The thermal treatment of typical mesoporous TiO_2 , employed to transform the pore walls from amorphous to crystalline usually leads to undesirable gain growth and a total collapse of ordered mesoporous network during the high calcinations temperature process [25–28]. Furthermore, the network of large pore mesoporous TiO_2 is more easily collapsed than that of smaller ones. Thus, the effects on the formation and thermal stability need further investigation, and the preparation of ordered mesoporous TiO_2 materials with high thermal stability, is still a great challenge [29,30]. Therefore, we designed the high thermostable ordered mesoporous $\text{SiO}_2\text{--TiO}_2$ composite. The induction of SiO_2 could inhibit crystal phase transform of TiO_2 from anatase to rutile, and maintain the ordered mesoporous structure of TiO_2 at the high calcinations temperature. The well-ordered mesoporous $\text{SiO}_2\text{--TiO}_2$ would improve photon utilization, organic molecule adsorption, and microorganism loading, and increase the surface reactive sites, due to its large surface area, ordered pore structure and large pore volume. Then, the macro/mesoporous $\text{SiO}_2\text{--TiO}_2$ /PUF carriers in PCBBR exhibited excellent photocatalytic and biocatalytic performance for the degradation of phenol and 2,4,5-TCP.

2. Materials and methods

2.1. Materials

All reagents, i.e., tetrabutyl titanate, tetraethyl orthosilicate, phenol, 2,4,5-trichlorophenol, absolute ethanol, concentrated nitric acid, and concentrated hydrochloric acid were of analytical grade and used without further purification. Pluronic P123 (triblock copolymer, $\text{HO}(\text{CH}_2\text{CH}_2\text{O})_{20}(\text{CH}_2\text{CH}(\text{CH}_3)\text{O})_{70}(\text{CH}_2\text{CH}_2\text{O})_{20}\text{H}$, abbreviated as $\text{EO}_{20}\text{PO}_{70}\text{EO}_{20}$, MW = 5800, BASF) was used as the pore-forming agent. Polyurethane foam (abbreviated as PUF, Beijing Siqingyuan Biological Technology Co., Ltd) had a three-dimensional macroporous network structure. The PUF carries were cubic in shape with an average length of 1 cm per side and an average pore size of 2 mm. Its density was 0.8 g/cm^3 , so the PUF could fluidize easily in the water under the normal aeration intensity.

2.2. Preparation of the ordered mesoporous $\text{SiO}_2\text{--TiO}_2$ photocatalyst

1 g of P123 was dissolved into 25 mL of deionized water, and then 1.85 mL of concentrated hydrochloric acid was added with stirring for 30 min. Subsequently, 2.3 mL of tetraethyl orthosilicate was added in the mixed solution with the constant magnetic stirring for 2 h as the solution A.

10 mL of tetrabutyl titanate was slowly added to 10 mL of absolute ethanol solution with the constant magnetic stirring as the solution B. 10 mL of deionized water was mixed with 40 mL absolute ethanol, and then 4 mL of concentrated nitric acid were added to the mixed solution as the solution C. Then, the solution C was slowly dropped to the solution B under the constant magnetic stirring. Then, the magnetic stirring was kept for 2 h to obtain a translucent solution. The translucent solution was gelled and aged for overnight, and then the obtained powders was washed at least three times by the deionized water and dried at 100°C for 1 h. Subsequently, the obtained powders were first calcined at 400°C with 2 h and then calcined at 500°C with 1 h. The pure TiO_2 as the contrastive sample was obtained. The above translucent solution was added into the solution A with the ultrasonic stirring for 5 min following by the magnetic stirring for 1 h. The resulting sol solution was gelled in an open petri dish at room temperature in air and 50–60% relative humidity (RH) for several weeks. Then, the as-prepared powders were washed at least three times by the deionized water and dried at 100°C for 1 h. Subsequently, the obtained powders were first calcined at 400°C with 2 h and then calcined at 800°C with 1 h. The ordered mesoporous $\text{SiO}_2\text{--TiO}_2$ composite with high thermostability as the photocatalyst was obtained. The weight ratio of $\text{TiO}_2\text{:SiO}_2$ was 3:7. When above solution was absence of tetrabutyl titanate, the pure SiO_2 as the contrastive sample was obtained.

2.3. Ordered mesoporous $\text{SiO}_2\text{--TiO}_2$ composite coating procedure

Firstly, 2 g of $\text{SiO}_2\text{--TiO}_2$ powders were dissolved into 20 mL absolute ethanol, and then 2 mL of concentrated nitric acid was added to the solution. After the ultrasonic vibration for 30 min at 80°C , 1:1 (v/v) ratio of PUF was added into the dispersed $\text{SiO}_2\text{--TiO}_2$ ethanol solution, followed by ultrasonic vibration for another 30 min. Subsequently, the $\text{SiO}_2\text{--TiO}_2$ coated PUF was taken out and dried at 60°C for 24 h. Finally, the mesoporous $\text{SiO}_2\text{--TiO}_2$ composite coated PUF carriers were obtained successfully as shown in Fig. 1. The weight ratio of coated PUF and fresh PUF was about 2:1.

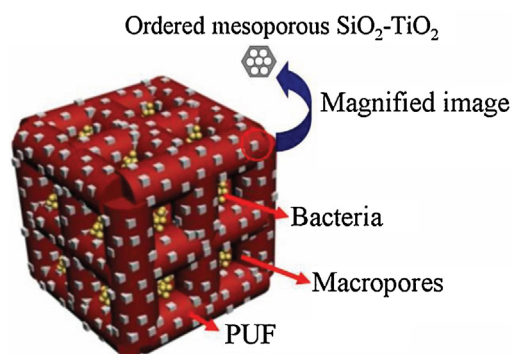


Fig. 1. Schematic view of the floating macro/mesoporous $\text{SiO}_2\text{-TiO}_2$ /PUF carrier.

2.4. Start-up of the photocatalytic circulating-bed biofilm reactor

The schematic diagram of experimental setup and PCBRR could be seen in Fig. S1. A laboratory scale quartz glass reactor with a liquid volume 1 L (inside diameter 8 cm \times height 20 cm) was used in the study. A quartz sleeve (diameter 3 cm) was placed in the middle of reactor, and a UV lamp (365 nm, 8 W) was in the quartz sleeve. The bottom of reactor was aerated, which could achieve fluidization. The outside of PCBRR was covered with aluminum foil in order to improve light utilization by reflection of light. The inoculated activated sludge was obtained from the CASS process tank of some Harbin Sewage Treatment Plant, oriented at 44°04'N and 125°42'E. It was acclimated by adding the phenol and 2,4,5-TCP by sequencing batch process, respectively. The concentration of phenol was increased gradually from 10 to 100 mg/L during the first acclimation stage, and the concentration of 2,4,5-TCP was increased gradually from 5 to 20 mg/L during the second acclimation stage. The experimental was carried out in the winter, and the PCBRR was placed in a cool room. The room temperature was kept at $12 \pm 2^\circ\text{C}$. The sole photocatalytic process was carried out by the PCBRR with the uninoculated $\text{SiO}_2\text{-TiO}_2$ /PUF carriers. The sole biological process was carried out by the PCBRR without the UV illumination.

2.5. Characterization

X-ray diffraction (XRD) was performed on a Bruker D8 Advance diffractometer by using $\text{Cu K}\alpha$ radiation ($\lambda = 1.5406 \text{ \AA}$). Raman measurements were performed with a Jobin Yvon HR 800 micro-Raman spectrometer at 457.9 nm. The laser beam was focused with a 50 \times objective lens to a ca. 1 μm spot on the surface of the sample. X-ray photoelectron spectroscopy (XPS) was conducted on a PHI-5700 ESCA instrument with Al-K α X-ray source. All binding energies were calibrated with respect to the C1s peak at 284.6 eV of the surface adventitious carbon. The Fourier transform infrared spectra (FT-IR) of the samples were collected with a PerkinElmer spectrum one system, using KBr as diluents. Scanning electron microscopy (SEM) micrographs were obtained with a Philips XL-30-ESEM-FEG instrument operating at 20 kV. Energy Dispersive X-ray Spectrometry (EDS) micro-analysis of the samples was performed. Transmission electron microscopy (TEM) was performed using a JEM-2100 electron microscope (JEOL, Japan). Nitrogen adsorption-desorption isotherms at 77 K were collected with an AUTOSORB-1 (Quantachrome Instruments) nitrogen adsorption apparatus. The Brunauer-Emmett-Teller (BET) equation was used to calculate the specific surface area. UV-vis diffuse reflectance spectroscopy (UV-vis DRS) was recorded on a Shimadzu UV-2500 spectrophotometer equipped with an integrating sphere, in which BaSO_4 was used as the reflectance sample. 2,4,5-TCP was measured by a high performance liquid chromatograph (HPLC, model: Agilent 1100, ASU) equipped with a diode array detector (DAD)

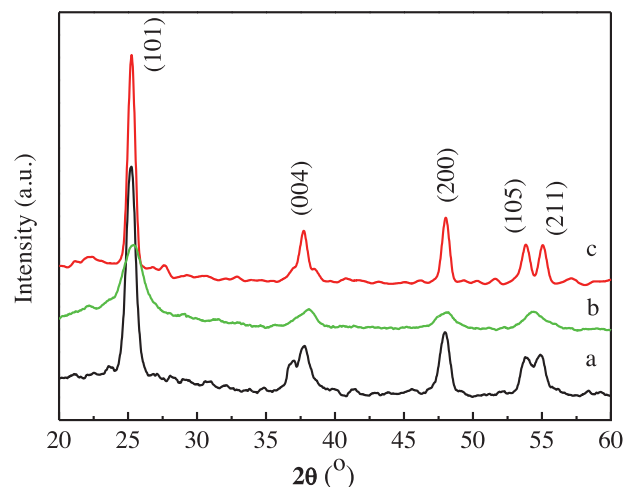


Fig. 2. XRD patterns of (a) the pure TiO_2 calcined at 500°C , (b) the $\text{SiO}_2\text{-TiO}_2$ calcined at 500°C , and (c) the $\text{SiO}_2\text{-TiO}_2$ calcined at 800°C , respectively.

with wavelength of 250 nm and ZORBAX SB-C18 column (5 μm , $4.6 \times 150 \text{ mm}$). The total organic carbon (TOC) analysis was carried out with a TOC-VCN (Shimadzu, Japan) analyzer with the minimum detection limit of 0.05 mg L^{-1} in accordance with standard methods [31].

3. Results and discussion

3.1. Structure and characterization of carriers

The anatase-to-rutile phase transformation in TiO_2 has attracted much attention because the phase structure of TiO_2 nanostructures largely determines their suitability for photocatalytic applications [32–34]. Thus, the crystallinity and crystal phase of the prepared samples are analyzed using XRD. Fig. 2 shows the XRD patterns of the pure TiO_2 calcined at 500°C , $\text{SiO}_2\text{-TiO}_2$ powders calcined at 500°C , and $\text{SiO}_2\text{-TiO}_2$ powders calcined at 800°C . In Fig. 2, five characteristic XRD peaks of anatase TiO_2 are observed at 25.2° , 37.8° , 48.1° , 53.9° , and 56.1° , which can be indexed to (1 0 1), (0 0 4), (2 0 0), (1 0 5), and (2 1 1), respectively. That is, the prepared $\text{SiO}_2\text{-TiO}_2$ can still retain the anatase phase and high crystallinity even after being calcined at 800°C . Both the d -spacing and the intensities are in good agreement with pure anatase TiO_2 , and with no trace of the rutile phase. In addition, the XRD peaks intensity of $\text{SiO}_2\text{-TiO}_2$ increase at 800°C calcinations comparing with the pure TiO_2 and $\text{SiO}_2\text{-TiO}_2$ at 500°C calcinations, indicating the improvement of crystallinity of anatase. As we known, when calcinations temperature is more than 500°C , the crystal phase of pure TiO_2 will transform from the anatase to rutile. However, the introduction of SiO_2 can inhibit the anatase-to-rutile phase transformation of TiO_2 at the higher calcinations temperature. From XRD analysis, there is no obvious crystalline SiO_2 characteristic peak, indicating that the SiO_2 still remain amorphous phase at 800°C calcinations. By applying the Scherrer equation to the anatase (1 0 1) diffraction peak, the average crystallite size of the synthesized $\text{SiO}_2\text{-TiO}_2$ and pure TiO_2 are calculated to be 6 nm and 25 nm, respectively. Comparing to the pure TiO_2 , the smaller crystallite size of the synthesized TiO_2 will favor the photocatalytic performance.

Raman spectroscopy is a promising method to evaluate crystalline TiO_2 . This technique allows the selection of a sampled area with several micrometers in size, and by scanning the sample surface the different Raman-active phases in the samples can be distinguished [35–37]. Therefore, in order to further confirm the crystallinity of the TiO_2 samples, Raman analysis is carried out. Fig. 3

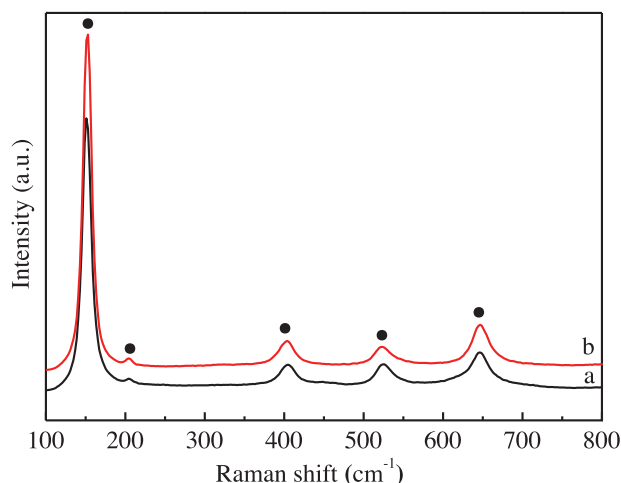


Fig. 3. Raman spectra of (a) the pure TiO_2 calcined at 500°C and (b) the $\text{SiO}_2\text{-TiO}_2$ calcined at 800°C .

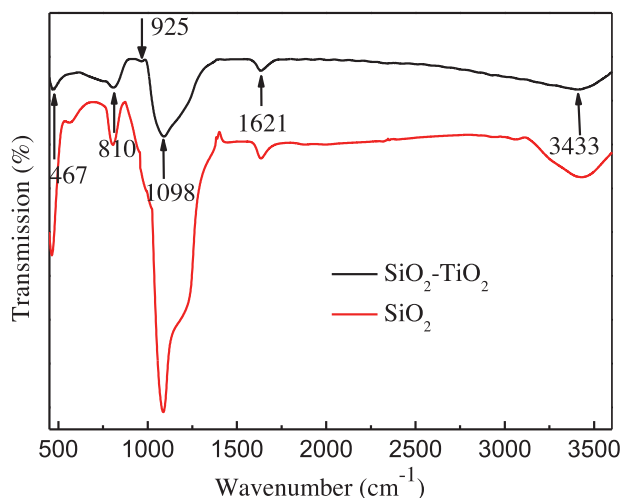


Fig. 4. FT-IR spectrum of the SiO_2 and $\text{SiO}_2\text{-TiO}_2$ calcined at 800°C .

shows the Raman spectra of the pure TiO_2 calcined at 500°C and prepared $\text{SiO}_2\text{-TiO}_2$ powders calcined at 800°C . In Fig. 3, five characteristic Raman peaks of anatase TiO_2 at 155, 206, 405, 530, and 642 cm^{-1} with high intensity are observed, which can be ascribed to E_g , E_g , B_{1g} , A_{1g} (B_{1g}), and E_g modes, respectively. There are no obvious Raman characteristic peaks of the rutile TiO_2 for the pure TiO_2 and prepared $\text{SiO}_2\text{-TiO}_2$, suggesting that main crystalline phase is anatase, which is in good agreement with the XRD results. Moreover, the Raman peaks intensity of prepared $\text{SiO}_2\text{-TiO}_2$ increase at 800°C calcinations, indicating the improvement of crystallinity of anatase, which is in good agreement with the XRD results.

The FT-IR spectrum of the $\text{SiO}_2\text{-TiO}_2$ is used to investigate the composition and structure of the resultant samples [38–40]. As shown in Fig. 4, the FT-IR peaks at about 3433 cm^{-1} and 1621 cm^{-1} are ascribed to the stretching vibrations of surface hydroxyl groups and the bending vibration of adsorbed water molecular, respectively. The FT-IR peak at about 467 cm^{-1} belongs to the stretching vibration of Ti–O in the TiO_2 lattice or Si–O in the SiO_2 lattice, and the peak at about 810 cm^{-1} is close related to asymmetric broad of Ti–O–Ti in the anatase phase TiO_2 lattice or Si–O–Si in the SiO_2 lattice. In addition, in Fig. 4 the $\text{SiO}_2\text{-TiO}_2$ possesses some signals due to SiO_2 , such as the asymmetric stretching of Si–O–Si at 1098 cm^{-1} and the vibration of Ti–O–Si at 925 cm^{-1} , which demonstrates the mixing and interaction between Si and Ti atoms. Furthermore, the

fact that the vibration of Si–O–Ti form at the 800°C calcinations temperature suggests that reactions indeed occur between Ti–OH and Si–OH.

XPS is a highly sensitive technique of surface analysis, and is an effective method to investigate the surface composition and chemical states of all kinds of solid samples [41–43]. In order to confirm the chemical state of Si, Ti and O atoms present in the $\text{SiO}_2\text{-TiO}_2$ composite, XPS is analyzed for the prepared photocatalyst. The Si, Ti and O elements are appeared in the survey spectrum of $\text{SiO}_2\text{-TiO}_2$ composite (Fig. 5a). The binding energy peaks of Si and Ti are shown in Fig. 5b and c, respectively. The binding energy of Ti 2p spectrum (Fig. 5b) shown at 464.6 and 458.8 eV which corresponds to Ti $2p_{1/2}$ and Ti $2p_{3/2}$, respectively. This result confirms the formation of pure anatase TiO_2 . The binding energy of Si 2p XPS spectrum (Fig. 5c) at 103.0 eV shows the formation of a Si–O–Si bond. Fig. 5d shows the XPS spectrum of the O 1s region taken on the surface of the $\text{SiO}_2\text{-TiO}_2$. The O 1s can be fitted by their curves appearing at 530.0, 532.0 and 534.4 eV, which can be attributed to Ti–O (530.0 eV), Si–O (532.0 eV) and OH (534.4 eV) components. Therefore, the obtained XPS results can be in good agreement with FT-IR analysis.

The morphology of the $\text{SiO}_2\text{-TiO}_2$ samples are further investigated by TEM. Fig. 6 shows the TEM and HRTEM image of ordered mesoporous $\text{SiO}_2\text{-TiO}_2$ powders after being calcined at 800°C . TEM image of $\text{SiO}_2\text{-TiO}_2$ powders after calcinations exhibits a 2D hexagonal mesostructure with P6 mm symmetry, which possesses highly ordered mesopores of about 5 nm in diameter (Fig. 6a). It also shows a high degree of periodicity of 2D hexagonal arrangements over large domains. From the HRTEM images (Fig. 6b), we can see that lattice fringes corresponding to the (1 0 1) ($d_{101} = 0.35\text{ nm}$) crystallographic planes of anatase TiO_2 are most frequently observed, which indicates the high crystallinity of the pore walls of mesoporous $\text{SiO}_2\text{-TiO}_2$. The nanocrystalline nature of anatase TiO_2 is well defined [44,45]. In addition, the existence of SiO_2 can firm the mesoporous structure of TiO_2 at the higher calcinations temperature. These results are consistent with the XRD and Raman findings. Such a high crystallinity of the mesoporous $\text{SiO}_2\text{-TiO}_2$ is highly desirable in photocatalysis.

Fig. 7 shows the N_2 adsorption–desorption isotherms and the corresponding Barrett–Joyner–Halenda (BJH) pore-size distribution plots of the $\text{SiO}_2\text{-TiO}_2$, respectively. At relatively high pressure (Fig. 7a), the curves exhibit type H3 hysteresis loops, which are attributed to type IV isotherms, and are representative of mesoporous materials. The synthesized mesoporous $\text{SiO}_2\text{-TiO}_2$ has a narrow BJH adsorption pore size distribution with a mean value of 5.26 nm (Fig. 7b), implying that the materials had very regular pore channels in the mesoporous region, which is consistent with the TEM observation. In addition, the prepared $\text{SiO}_2\text{-TiO}_2$ possesses a specific BET surface area $224.97\text{ m}^2\text{ g}^{-1}$ and a total pore volume of $0.3084\text{ cm}^3\text{ g}^{-1}$. Due to the large density of crystalline TiO_2 , this obtained BET surface area is very high for $\text{SiO}_2\text{-TiO}_2$ with high crystallinity [46,47]. Therefore, the relative high surface area and the integrated porous structure will be beneficial for the subsequent adsorption and photocatalytic reactions.

The surface morphology of the carriers is investigated using SEM analysis, as shown in Fig. 8. Fig. 8a and d indicate that the surface of the uncoated PUF is very smooth. However, with the $\text{SiO}_2\text{-TiO}_2$ coated PUF, uniformly distributed $\text{SiO}_2\text{-TiO}_2$ which is agglomerated from the nanosized $\text{SiO}_2\text{-TiO}_2$ particles are clearly seen on the surface, as shown in Fig. 8b and e. It suggests that the $\text{SiO}_2\text{-TiO}_2$ is coated on the PUF surface successfully. The insets of Fig. 8a and b show that the color of pure PUF is yellow, while the $\text{SiO}_2\text{-TiO}_2$ coated PUF turns to white. The macroporous structure of PUF and $\text{SiO}_2\text{-TiO}_2\text{/PUF}$ can be observed by visual inspection. In addition, after microorganisms are inoculated within the carrier, the interior surfaces of carriers are examined by SEM as shown in Fig. 8e and f.

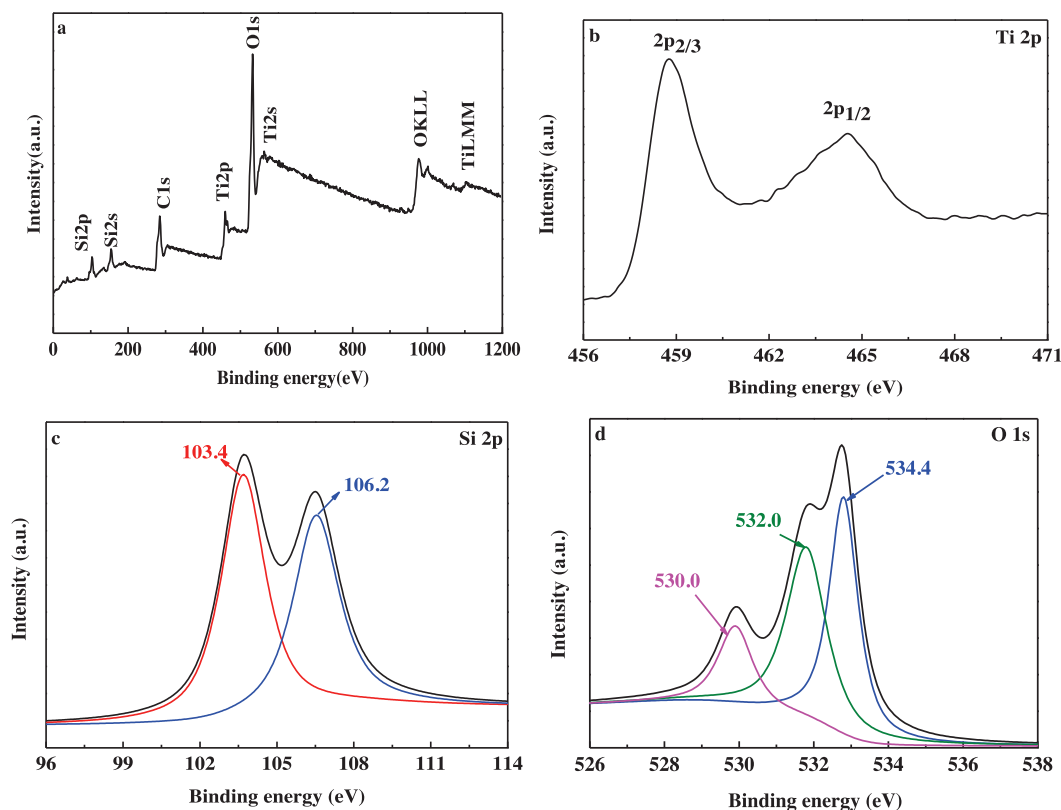


Fig. 5. XPS spectra of (a) $\text{SiO}_2\text{-TiO}_2$, (b) Ti 2p, (c) Si 2p and (d) O 1s.

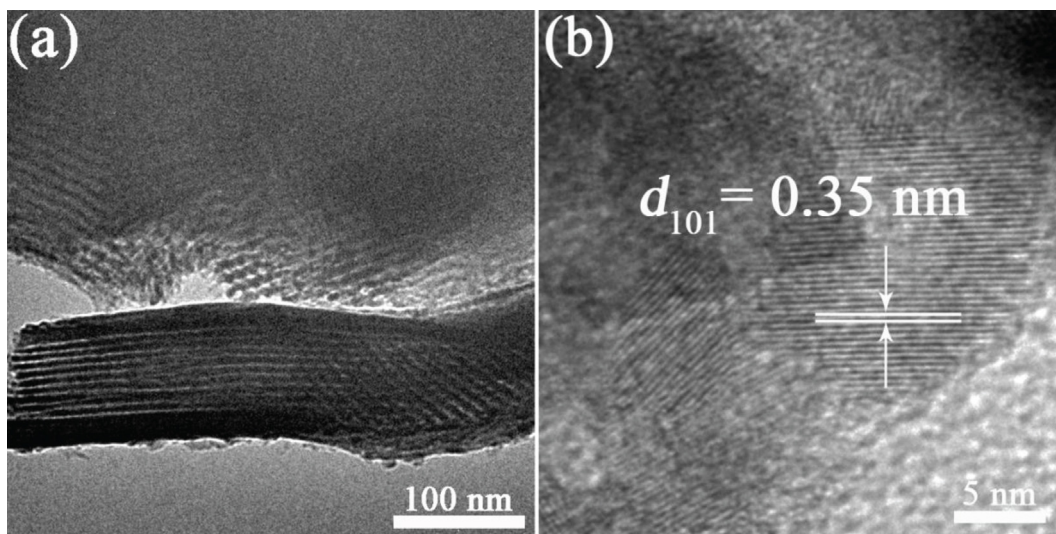


Fig. 6. TEM (a) and HRTEM (b) images of ordered mesoporous $\text{SiO}_2\text{-TiO}_2$ powders prepared at 800°C (anatase: $d_{101} = 0.35\text{ nm}$).

It can be found that some sphaerita and short bacilli remains in the macropores, indicating the microorganisms are inoculated inside the carriers successfully. The insets of Fig. 8c show that the carriers of $\text{SiO}_2\text{-TiO}_2$ coated PUF are indeed loaded the bacterium. The biofilm inside the carriers can shade the UV irradiation and photocatalytic oxidation, and has active in removing the biodegradable organic pollutants [22,43].

In addition, the uncoated PUF and the $\text{SiO}_2\text{-TiO}_2$ coated PUF samples are further characterized by the EDS in Fig. S2. For pure PUF sample, the C, N, and O elements are clearly detected in the Fig. S2a. While for the $\text{SiO}_2\text{-TiO}_2$ coated PUF sample, the signals for Ti and Si element were observed in Fig. S2b, confirming

the $\text{SiO}_2\text{-TiO}_2$ is coated successfully [48,49]. After coating, the N element is disappeared, because the surface of PUF is covered with $\text{SiO}_2\text{-TiO}_2$ powder. Within the detection limit of EDS analysis in Fig. S2, no other impurity is detected. Furthermore, the optical property of pure TiO_2 calcined at 500°C and $\text{SiO}_2\text{-TiO}_2$ calcined at 800°C has been measured by UV–vis diffuse reflectance spectra in Fig. S3. The band gap of pure TiO_2 and $\text{SiO}_2\text{-TiO}_2$ are 3.07 and 3.02 eV, respectively. It indicates that the introduction of SiO_2 can not reduce the band gap of $\text{SiO}_2\text{-TiO}_2$ obviously. The prepared $\text{SiO}_2\text{-TiO}_2\text{/PUF}$ is also tested by XRD, FT-IR, and N_2 adsorption–desorption isotherms in Fig. S4–S7. After coat-

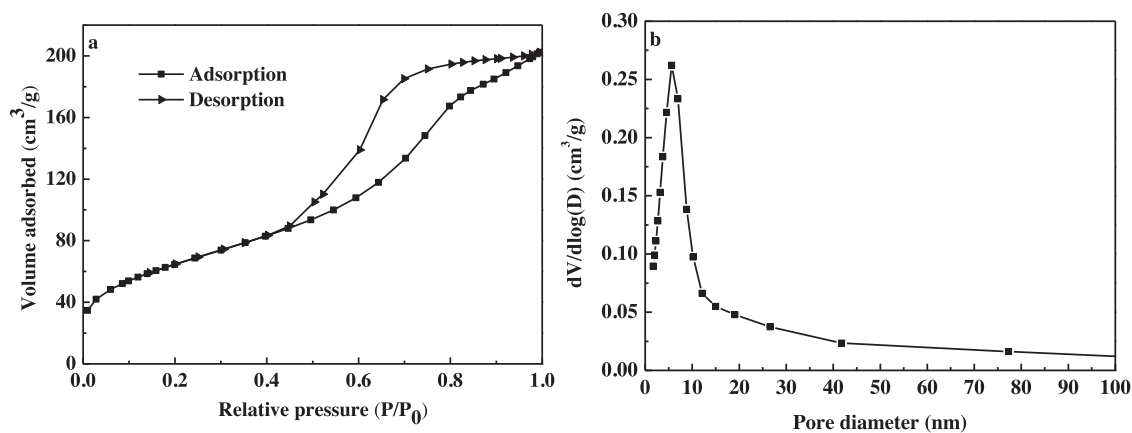


Fig. 7. N₂ adsorption-desorption isotherms (a) and BJH pore size distribution (b) of SiO₂-TiO₂ calcined at 800 °C.

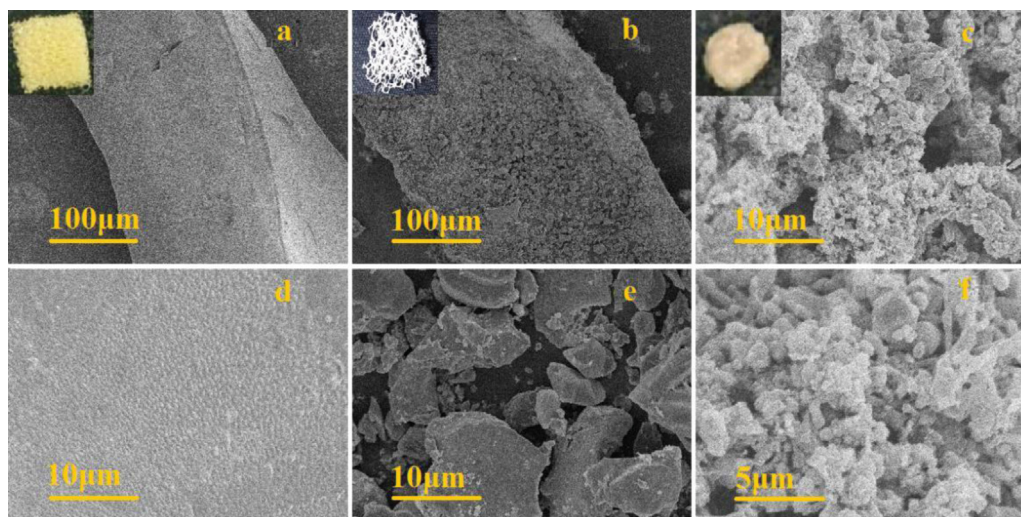


Fig. 8. SEM images of the PUF (a and c), the SiO₂-TiO₂/PUF (view on outside) (b and d), and the biofilms on SiO₂-TiO₂/PUF (view on inside) (e and f).

ing procedure, the performance of SiO₂-TiO₂ powder can remain unchanged.

3.2. Performance of SiO₂-TiO₂/PUF carriers by PCBBR

The start-up of photocatalytic circulating-bed biofilm reactor is with different initial concentration of the phenol and 2,4,5-TCP, respectively. Fig. 9 shows the evolution of influent pollutant concentration at every sequencing batch term. One sequencing batch term corresponding 10 h of hydraulic retention time (HRT), and the phenol and 2,4,5-TCP concentration of influent is increased step by step from 10 to 100 mg/L and from 5 to 20 mg/L after every two HRT terms, respectively. In Fig. 9a, the phenol removal at the second HRT term is better than the first HRT term in each designated initial phenol concentration of influent, indicating the bacterium acclimate the pollutants gradually. When initial phenol concentration of influent is raised, the phenol concentration of effluent also is increased. It is reasonable that the higher phenol concentration of effluent can be obtained with the organic loading increasing for the microbiological treatment. When initial phenol concentration of influent is controlled at 100 mg/L, the phenol concentration of effluent stabilizes at 71.9 mg/L in the second HRT term. It is indicated that bacteria is acclimated completely for the phenol degradation. In Fig. 9b, the 2,4,5-TCP removal can be obtained the same degradation regularities like the phenol. When initial 2,4,5-TCP concentration of influent is controlled at 20 mg/L, the 2,4,5-TCP

concentration of effluent stabilizes at 15.7 mg/L in the second HRT term. It is indicated that bacteria is acclimated completely for the 2,4,5-TCP degradation. However, comparing to phenol, 7.1 and 5.8 mg/L of phenol effluent can be obtained at each HRT terms for initial 20 mg/L of phenol influent, respectively, indicating the 2,4,5-TCP is more difficult to be biodegraded than phenol.

The photocatalytic degradation, biological degradation and photocatalytic degradation coupled biological degradation process is denoted as P, B, and P&B, respectively. Fig. 10 shows the phenol removal in sequencing batch PCBBR with different initial phenol concentrations. In Fig. 10a, when initial phenol concentration of influent increases from 20 to 100 mg/L, the phenol concentration of effluent is from 3.5 to 38.7 mg/L after 5 h of reaction time by the P process, respectively. The high specific surface and ordered mesoporous structure of SiO₂-TiO₂ will be favor of the pollutants adsorption and photon utility. The high crystallinity and anatase phase of TiO₂ will be favor of photocatalysis. In addition, the higher concentration of influent corresponds to the higher concentration of effluent. It indicates the more organic pollutants need be degraded by photocatalysis for the higher concentration of influent. In Fig. 10b, when initial phenol concentration of influent is 20, 40, 60, 80 and 100 mg/L, the phenol concentration of effluent is removed completely at 1, 1, 1, 2 and 3 h of reaction time by the P&B process, respectively. It indicates the photocatalysis coupled biodegradation can further improve the high initial concentration of phenol removal.

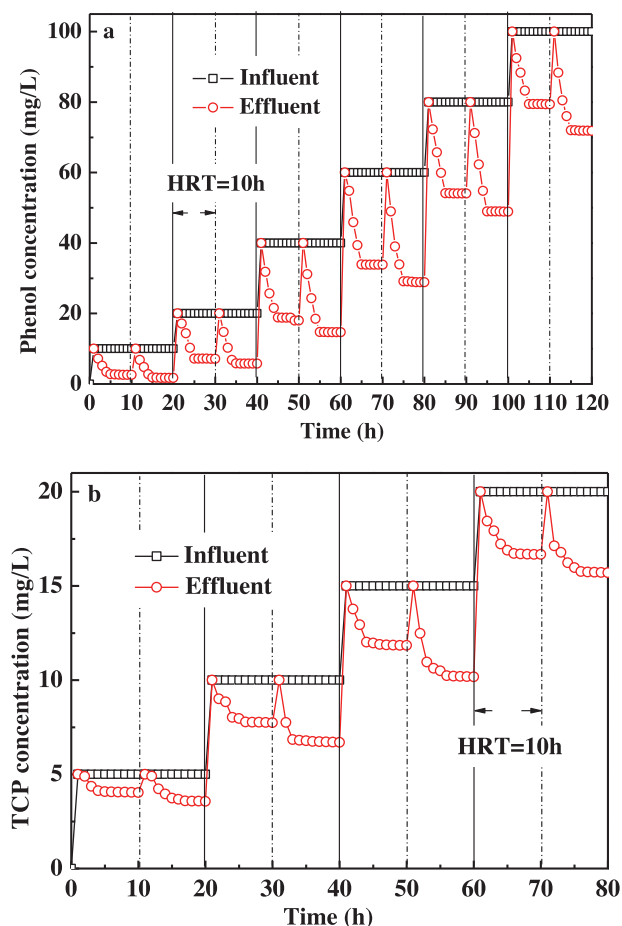


Fig. 9. Effect of influent pollutant concentration at every sequencing batch term: (a) phenol and (b) 2,4,5-TCP.

Fig. 11 shows the phenol removal in sequencing batch PCBBR with different initial 2,4,5-TCP concentrations. In Fig. 11a, when initial 2,4,5-TCP concentration of influent increases from 5 to 20 mg/L, the 2,4,5-TCP concentration of effluent is from 0.4 to 5.7 mg/L after 6 h of reaction time by the P process, respectively. The photocatalytic degradation trend of 2,4,5-TCP is similar with phenol. That is, the higher concentration of influent corresponds to the higher concentration of effluent. Comparing the initial 20 mg/L of phenol with 2,4,5-TCP sample, the 2,4,5-TCP concentration of effluent is higher than phenol, indicating that 2,4,5-TCP is indeed difficult to

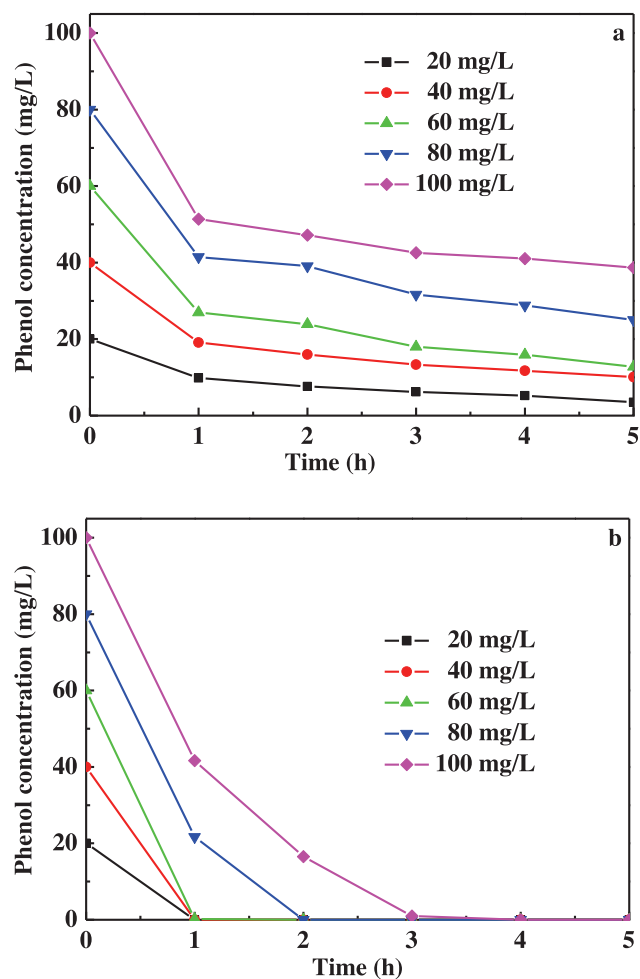


Fig. 10. Phenol removal in sequencing batch PCBBR with different initial phenol concentrations by the P (a) and P&B (b) process, respectively.

be degraded than phenol owing to its more complicated molecule structure. In Fig. 11b, when initial 2,4,5-TCP concentration of influent is 5, 10, 15 and 20 mg/L, the 2,4,5-TCP concentration of effluent is removed completely at 4, 4, 5 and 6 h of reaction time by the P&B process, respectively. It also indicates the photocatalysis coupled biodegradation can further improve the 2,4,5-TCP removal. According to the reports, the reason why these refractory contaminants can be removed quickly is mainly owing to the synergy mecha-

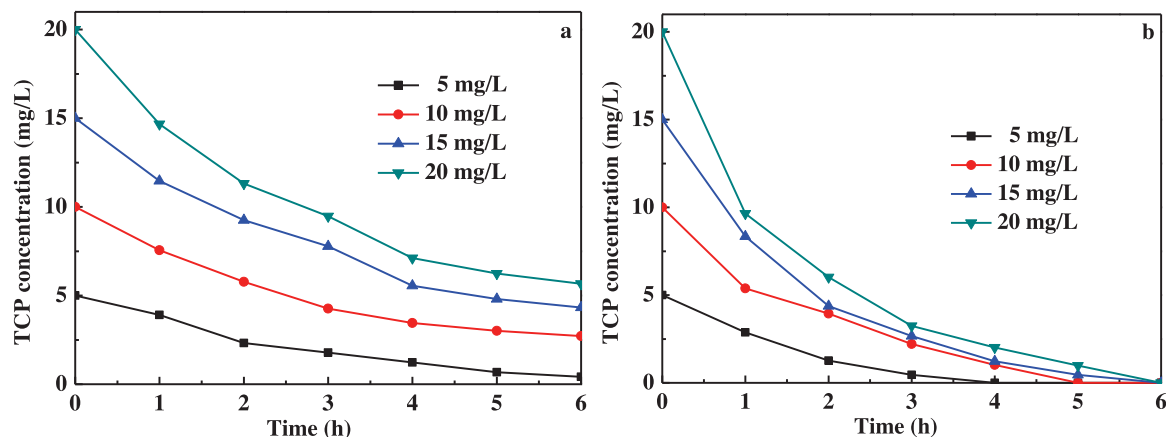


Fig. 11. 2,4,5-TCP removal in sequencing batch PCBBR with different initial 2,4,5-TCP concentrations by the P (a) and P&B (b) process, respectively.

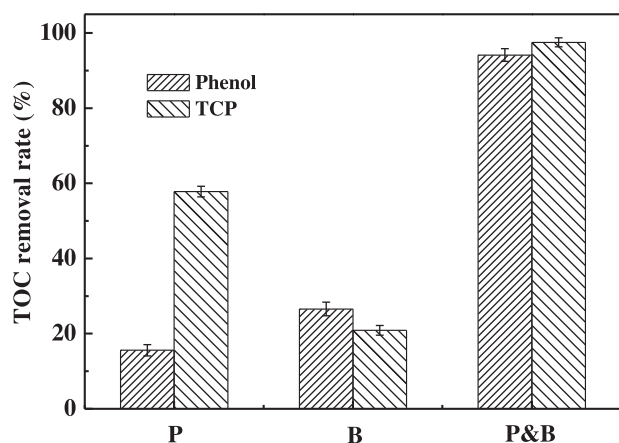


Fig. 12. TOC removal on the 20 mg/L of phenol and 2,4,5-TCP by P, B and P&B process with 1 h of HRT and 6 h of HRT, respectively.

nism of adsorption, photolysis, photocatalysis and biocatalysis in the PCBBR [21,22]. In addition, comparing with the pure TiO_2 /PUF carriers, the performance of SiO_2 - TiO_2 /PUF is overwhelming for different initial phenol and 2,4,5-TCP concentration removal as shown in Fig. S8.

The mineralization of phenol and 2,4,5-TCP is inspected by TOC analysis. Fig. 12 shows the TOC removal rate on the initial 20 mg/L of phenol and 2,4,5-TCP by P, B and P&B process with 1 h of HRT and 6 h of HRT, respectively. In Fig. 12, 15.6, 26.6 and 94.1% of TOC removal rate can be obtained for the initial 20 mg/L of phenol by P, B and P&B process with 1 h of HRT, respectively. It indicates the phenol is easier to be degraded by biological treatment than photocatalysis. And the synergetic efficiency between photocatalysis and biological treatment is better than the sole process efficiency for the phenol removal. From Fig. 12, 57.8, 20.9 and 97.5% of TOC removal rate can be obtained for the initial 20 mg/L of 2,4,5-TCP by P, B and P&B process with 6 h of HRT, respectively. It indicates the 2,4,5-TCP is difficult to be degraded by the biological treatment than photocatalysis. Similarly, the synergetic efficiency between photocatalysis and biological treatment is also better than the sole efficiency for the 2,4,5-TCP removal. In addition, the TOC removal rate of 2,4,5-TCP is higher than phenol by P process, owing to the longer HRT of 2,4,5-TCP. These results indicate the high thermostable ordered mesoporous SiO_2 - TiO_2 coated circulating-bed biofilm reactor can mineralize the refractory pollutants efficiently.

Furthermore, the XRD, N_2 adsorption-desorption isotherms and degradation activity test by P&B process for SiO_2 - TiO_2 at different calcinations temperature can be seen in Fig. S4–S6 and S9. In Fig. S4, it indicates the crystallinity of SiO_2 - TiO_2 is improved with the calcined temperature increasing from 700 to 900 °C. However, from the N_2 adsorption-desorption isotherms results, the BET specific surface area of SiO_2 - TiO_2 calcined at 700, 800 and 900 °C is 290.20, 224.97 and 27.65 $\text{m}^2 \text{g}^{-1}$, respectively. It indicates the BET specific surface area of SiO_2 - TiO_2 is decreased with the calcined temperature increasing from 700 to 900 °C. From Fig. 12 and Fig. S9, the SiO_2 - TiO_2 calcined at 800 °C shows the best activity comparing to the samples calcined at 700 and 900 °C. The obtained results exhibits the SiO_2 - TiO_2 has a optimum calcinations temperature at 800 °C, which can obtain both higher TiO_2 crystallinity than 700 °C calcinations and higher BET specific surface area than 900 °C calcinations.

4. Conclusions

The high thermostable ordered mesoporous SiO_2 - TiO_2 was coated macroporous PUF, and PCBBR was prepared successfully.

The induction of SiO_2 could inhibit crystal phase transform of TiO_2 from anatase to rutile, and firm the ordered mesoporous structure of TiO_2 at high calcinations temperature. The macro/mesoporous SiO_2 - TiO_2 /PUF as the biofilm carriers showed the excellent photocatalytic and biocatalytic performance in the PCBBR. 100 mg/L of phenol and 20 mg/L of 2,4,5-TCP could be removed completely with 3 h and 6 h of HRT, respectively. Compared with P and B, intimate coupling of P&B was obviously superior for the phenol and 2,4,5-TCP removal due to the synergetic effect between photocatalysis and biodegradation. Therefore, this high efficient photocatalytic coupled biological technology with the high performance biofilm carriers will likely trigger a strong interest in this filed of research.

Acknowledgements

We gratefully acknowledge the support of this research by the National Natural Science Foundation of China (21376065, 81302511, and 81202282), the Natural Science Foundation of Heilongjiang Province (QC2012C001 and QC2013C079), the Heilongjiang Postdoctoral Startup Fund (LBH-Q14135), the Program for New Century Excellent Talents in University of Heilongjiang Province (1253-NCET-020), and the Scientific Research Fund of Heilongjiang Provincial Education Department (12521226).

Appendix A. Supplementary data

Supplementary data associated with this article can be found, in the online version, at <http://dx.doi.org/10.1016/j.apcatb.2015.07.002>

References

- [1] M.C.M. van Loosdrecht, D. Brdjanovic, *Science* 344 (2014) 1452–1453.
- [2] I. Zucker, Y. Lester, D. Avisar, U. Hübner, M. Jekel, Y. Weinberger, H. Mamane, *Environ. Sci. Technol.* 49 (2015) 301–308.
- [3] Z. Xing, D. Sun, X. Yu, J. Zou, W. Zhou, *Environ. Prog. Sustainable Energy* 33 (2014) 170–177.
- [4] Z. Wu, P.A. Webley, D. Zhao, *J. Mater. Chem.* 22 (2012) 11379–11389.
- [5] S.Y. Yang, W. Choi, H. Park, *ACS Appl. Mater. Interfaces* 7 (2015) 1907–1914.
- [6] R. Su, R. Tiruvalam, Q. He, N. Dimitratos, L. Kesavan, C. Hammond, J.A. Lopez-Sanchez, R. Bechstein, C.J. Kiely, G.J. Hutchings, F. Besenbacher, *ACS Nano* 6 (2012) 6284–6292.
- [7] J. Pan, B. Wang, J. Dai, X. Dai, H. Hang, H. Ou, Y. Yan, *J. Mater. Chem.* 22 (2012) 3360–3369.
- [8] A.D. Pereira, C.D. Leal, M.F. Dias, C. Etchebehere, C.A.L. Chernicharo, J.C. Araújo, *Bioresour. Technol.* 166 (2014) 103–111.
- [9] D. Pérez-González, J. Gómez, R. Beristain-Cardoso, *Bioresour. Technol.* 120 (2012) 194–198.
- [10] Y. Wang, Y. Zhang, G. Zhao, H. Tian, H. Shi, T. Zhou, *ACS Appl. Mater. Interfaces* 4 (2012) 3965–3972.
- [11] G. Zhang, G. Kim, W. Choi, *Energy Environ. Sci.* 7 (2014) 954–966.
- [12] W.Q. Wu, Y.F. Xu, H.S. Rao, C.Y. Su, D.B. Kuang, *J. Am. Chem. Soc.* 136 (2014) 6437–6445.
- [13] Z. Xing, J. Li, Q. Wang, W. Zhou, G. Tian, K. Pan, C. Tian, J. Zou, H. Fu, *Eur. J. Inorg. Chem.* 2013 (2013) 2411–2417.
- [14] Z. Bian, T. Tachikawa, P. Zhang, M. Fujitsuka, T. Majima, *Nat. Commun.* 5 (2014) 3038.
- [15] Z. Bian, T. Tachikawa, P. Zhang, M. Fujitsuka, T. Majima, *J. Am. Chem. Soc.* 136 (2014) 458–465.
- [16] B. Liu, Y. Sun, X. Wang, L. Zhang, D. Wang, Z. Fu, Y. Lin, T. Xie, *J. Mater. Chem. A* 3 (2015) 4445–4452.
- [17] J. Shang, W. Hao, X. Lv, T. Wang, X. Wang, Y. Du, S. Dou, T. Xie, D. Wang, J. Wang, *ACS Catal.* 4 (2014) 954–961.
- [18] Y. Wang, Y. Zhang, G. Zhao, H. Tian, H. Shi, T. Zhou, *ACS Appl. Mater. Interfaces* 4 (2012) 3965–3972.
- [19] G. Li, S. Park, B.E. Rittmann, *Water Res.* 46 (2012) 6489–6496.
- [20] M.D. Marsoslek, M.J. Kirisits, K.A. Gray, B.E. Rittmann, *Water Res.* 50 (2014) 59–69.
- [21] Y. Zhang, X. Sun, L. Chen, B.E. Rittmann, *Biodegradation* 23 (2012) 189–198.
- [22] G. Li, S. Park, D.W. Kang, R. Krajmalnik-Brown, B.E. Rittmann, *Environ. Sci. Technol.* 45 (2011) 8359–8367.
- [23] Z. Xing, W. Zhou, F. Du, L. Zhang, Z. Li, H. Zhang, W. Li, *ACS Appl. Mater. Interfaces* 6 (2014) 16653–16660.
- [24] Z. Xing, W. Zhou, F. Du, Y. Qu, G. Tian, K. Pan, C. Tian, H. Fu, *Dalton Trans.* 43 (2014) 790–798.

- [25] W. Zhou, F. Sun, K. Pan, G. Tian, B. Jiang, Z. Ren, C. Tian, H. Fu, *Adv. Funct. Mater.* 21 (2011) 1922–1930.
- [26] M. Wang, Z. Sun, Q. Yue, J. Yang, X. Wang, Y. Deng, C. Yu, D. Zhao, *J. Am. Chem. Soc.* 136 (2014) 1884–1892.
- [27] Y. Li, W. Luo, N. Qin, J. Dong, J. Wei, W. Li, S. Feng, J. Chen, J. Xu, A.A. Elzatahry, M.H. Es-Saheb, Y. Deng, D. Zhao, *Angew. Chem. Int. Ed.* 53 (2014) 9035–9040.
- [28] Y. Deng, J. Wei, Z. Sun, D. Zhao, *Chem. Soc. Rev.* 42 (2013) 4054–4070.
- [29] W. Zhou, W. Li, J.Q. Wang, Y. Qu, Y. Yang, Y. Xie, K. Zhang, L. Wang, H. Fu, D. Zhao, *J. Am. Chem. Soc.* 136 (2014) 9280–9283.
- [30] W. Zhou, H. Fu, *ChemCatChem* 5 (2013) 885–894.
- [31] APHA, *Standard Methods for the Examination of Water and Wastewater*, 20th Edition, American Public Health Association, New York, 1998.
- [32] P. Zhang, Y. Yu, E. Wang, J. Wang, J. Yao, Y. Cao, *ACS Appl. Mater. Interfaces* 6 (2014) 4622–4629.
- [33] K.T. Kim, G. Ali, K.Y. Chung, C.S. Yoon, H. Yashiro, Y.K. Sun, J. Lu, K. Amine, S.T. Myung, *Nano Lett.* 14 (2014) 416–422.
- [34] Y. Luo, J. Huang, *Chem. Eur. J.* 21 (2015) 2568–2575.
- [35] M.T.N. Dinh, P. Rajbhandari, C. Lancelot, P. Blanchard, C. Lamonier, M. Bonne, S. Royer, F. Dumeignil, E. Payen, *ChemCatChem* 6 (2014) 328–338.
- [36] Z. Li, S. Cong, Y. Xu, *ACS Catal.* 4 (2014) 3273–3280.
- [37] D. Carboni, D. Marongiu, P. Rassu, A. Pinna, H. Amenitsch, M. Casula, A. Marcelli, G. Cibin, P. Falcaro, L. Malfatti, P. Innocenzi, *J. Phys. Chem. C* 118 (2014) 12000–12009.
- [38] V. Etacheri, M.K. Seery, S.J. Hinder, S.C. Pillai, *Adv. Funct. Mater.* 21 (2011) 3744–3752.
- [39] X. Li, J. He, *ACS Appl. Mater. Interfaces* 5 (2013) 5282–5290.
- [40] P. Xu, S. Guo, H. Yu, X. Li, *Small* 10 (2014) 2404–2412.
- [41] S. Flaig, J. Akbarzadeh, P. Dolcet, S. Gross, H. Peterlik, N. Hüsing, *Chem. Eur. J.* 20 (2014) 17409–17419.
- [42] S. Zhang, M. Han, J. Zhang, Y. Li, Z. Hu, J. Chu, *ACS Appl. Mater. Interfaces* 5 (2013) 3191–3198.
- [43] M.D. Marsolek, C.I. Torres, M. Hausner, B.E. Rittmann, *Biotechnol. Bioeng.* 101 (2008) 83–92.
- [44] D.W. Lee, M.H. Jin, C.B. Lee, D. Oh, S.K. Ryi, J.S. Park, J.S. Bae, Y.J. Lee, S.J. Park, Y.C. Choi, *Nanoscale* 6 (2014) 3483–3487.
- [45] F. Shan, X. Lu, Q. Zhang, J. Wu, Y. Wang, F. Bian, Q. Lu, Z. Fei, P.J. Dyson, *J. Am. Chem. Soc.* 134 (2012) 20238–20241.
- [46] Y. Zhang, Z. Zhao, J. Chen, L. Cheng, J. Chang, W. Sheng, C. Hu, S. Cao, *Appl. Catal. B* 165 (2015) 715–722.
- [47] G. Wang, X. Zhu, J. Yu, *J. Power Sources* 278 (2015) 344–351.
- [48] D.S. Bhachu, S. Sathasivam, G. Sankar, D.O. Scanlon, G. Cibin, C.J. Carmalt, I.P. Parkin, G.W. Watson, S.M. Bawaked, A.Y. Obaid, S. Al-Thabaiti, S.N. Basahel, *Adv. Funct. Mater.* 24 (2014) 5075–5085.
- [49] S. Porsgaard, L.R. Merte, L.K. Ono, F. Behafarid, J. Matos, S. Helveg, M. Salmeron, B.R. Cuenya, F. Besenbacher, *ACS Nano* 6 (2012) 10743–10749.